Analog Modulation of 1.55μm Vertical-Cavity Lasers

Joachim Piprek*[a], Koichi Takiguchi[a,b], Alexis Black[c], Patrick Abraham[a],
Adrian Keating[a], Volkan Kaman[a], Sheng Zhang[a], and John E. Bowers[a]

[a] Electrical and Computer Engineering Department, University of California, Santa Barbara, CA 93106
[b] on leave from NTT Opto-electronics Labs., Tokai, Naka, Ibaraki 319-1193, Japan
[c] Materials Department, University of California, Santa Barbara, CA 93106

ABSTRACT

We analyze the performance of InP/GaAs fused 1.55μm vertical-cavity lasers (VCLs) under analog modulation. Our VCLs employ a strain-compensated InGaAsP/InP multi-quantum well (MQW) active region sandwiched between two AlGaAs/GaAs distributed Bragg reflectors (DBRs). The first AlGaAs layer of the p-doped top mirror is laterally oxidized for optical and electrical confinement. These devices exhibit the lowest threshold current as well as the highest temperature of continuous-wave operation of any electrically pumped long-wavelength VCL. Two different device designs are investigated and compared. Reduction of the MQW barrier strain and enhancement of the optical index guiding by the oxide layer lead to an improvement of VCL performance. However, parasitic effects limit the modulation bandwidth. Higher order harmonic distortion is measured and simulated using a rate equation model. The model includes a non-linear gain function, gain compression, spontaneous emission and Auger recombination as well as carrier density dependent absorption in the quantum wells which reduces the differential gain. The good agreement between measurement and simulation indicates that electron-photon interaction within the quantum wells dominates the non-linear distortion. Multiple higher order response peaks are measured and reproduced by the model.

Keywords: long-wavelength laser diode, vertical-cavity laser, analog modulation, harmonic distortion, rate-equation model, small signal analysis

1. INTRODUCTION

Long-wavelength vertical-cavity lasers (VCLs) operating at 1.3μm or 1.55μm wavelength are potentially low cost light sources for optical communication systems. The lowest threshold current as well as the highest temperature of continuous-wave (cw) operation has been achieved using AlGaAs/GaAs distributed Bragg reflectors (DBRs) that are fused to InGaAsP/InP active regions. At room temperature, our double fused 1.55μm VCLs have shown threshold currents of 0.8mA,[1] 4.6 GHz modulation bandwidth,[2] a modulation current efficiency factor MCEF of 3.3 GHz/√mA,[2] 51dB side mode suppression ratio,[3] and digital transmission rates of 2.5Gb/s over 200 km fiber.[3] First analog transmission experiments using those 1.55μm VCLs recently showed low 3rd order intermodulation distortion with 80 dB $Hz^{2/3}$ spurious free dynamic range.[4] However, more investigations are required to optimize long-wavelength VCLs for high-speed applications. 1.55μm in-plane laser diodes have achieved up to 30 GHz modulation bandwidth (MCEF=1.2 GHz/√mA).[5] 970nm VCLs with GaAs based active region have shown a record-high modulation efficiency (MCEF=16.8 GHz/√mA)[6] which demonstrates the advantage of smaller active regions compared to in-plane lasers. 850nm VCLs with reduced parasitic effects reached 21 GHz modulation bandwidth.[7] Intrinsic resonance frequencies up to 71 GHz have been measured on 960nm VCLs.[8]

In this paper, we study the analog modulation performance of a new generation of double-fused 1.55μm VCLs.[9] Detailed comparison to previous amplitude modulation results[1] reveals which design improvements are most important. We also

* Correspondence: Email: piprek@ece.ucsb.edu; Telephone: 805-893-4051; WWW: http://eci.ucsb.edu/~piprek

Part of the SPIE Conference on Vertical-Cavity Surface-Emitting
Lasers III • San Jose, California • January 1999
SPIE Vol. 3627 • 0277-786X/99/$10.00

evaluate 2nd and 3rd order harmonic distortions of the laser output. Those non-linear effects generate additional output signals at double and triple the input modulation frequency, respectively. This is undesirable in many applications, e.g., in cable TV systems. For typical 80 channel 60-540MHz systems, the composite 2nd order harmonic distortion must not exceed –60dB.[10] Sect. 2 gives the design differences between the two device generations investigated. In Sect. 3, we describe a rate equation model that is applied to predict differences in the first and higher order harmonic response. Experimental results on modulation response and harmonic distortions are presented and analyzed in Sect. 4.

2. DEVICES

Analog modulation experiments are performed on two different types of double-fused 1.55μm VCLs which are referred to as device A and B in the following. In both the devices optical and electrical confinement is obtained by lateral oxidation within the first AlGaAs layer of the top p-doped GaAs/AlGaAs DBR (Fig. 1).

The previous device A is a bottom-emitting VCL (Fig. 1a).[1] The top p-doped (Beryllium) DBR contains 30.5 periods of $Al_{0.67}Ga_{0.33}As/GaAs$, the bottom n-DBR is a 24 period AlAs/GaAs stack. The active region includes seven strained (1% compressive) $In_{0.77}Ga_{0.23}As_{0.78}P_{0.22}$ quantum wells (7nm wide) with six $In_{0.54}Ga_{0.46}As_{0.78}P_{0.22}$ strain compensating barriers (0.9% tensile strain, 8.6nm thick). The MQW is sandwiched between 300 nm thick InP layers to complete a three halves wavelength cavity. Peak photoluminescence (PL) intensity was measured to be at 1548 nm before wafer fusion and the lasing wavelength of the final device is 1544nm at room temperature, indicating little gain offset from the emission wavelength. The oxide layer is about 20nm thick and it is placed near the null of the standing optical wave.

Our new device B is a top emitting VCL (Fig. 1b).[9] The top p-doped (Carbon) mirror consists of 25.5 quarter wave periods of $Al_{0.9}Ga_{0.1}As/GaAs$. The bottom mirror is an undoped 30 period GaAs/AlAs quarter wave stack. The active region consists of six 7 nm 1%-strained $In_{0.76}Ga_{0.24}As_{0.82}P_{0.18}$ quantum wells with seven 7 nm thick unstrained $In_{0.80}Ga_{0.20}As_{0.43}P_{0.57}$ barriers. The band gap wavelength of the barriers is 1180nm. On either side of the active region is a tensile strained $In_{0.9}Ga_{0.1}P$ layer and a 300nm InP cladding. The InGaP barriers serve both to compensate the compressive strain in the QWs and increase the confinement energy of the electrons in the active region by 30meV relative to InP. The MQW PL peak was 1542nm before fusion and lasing is observed at 1507nm, indicating large gain offset at room temperature. The tapered oxide layer is up to 40nm thick and it is placed further away from the optical null than in device A.

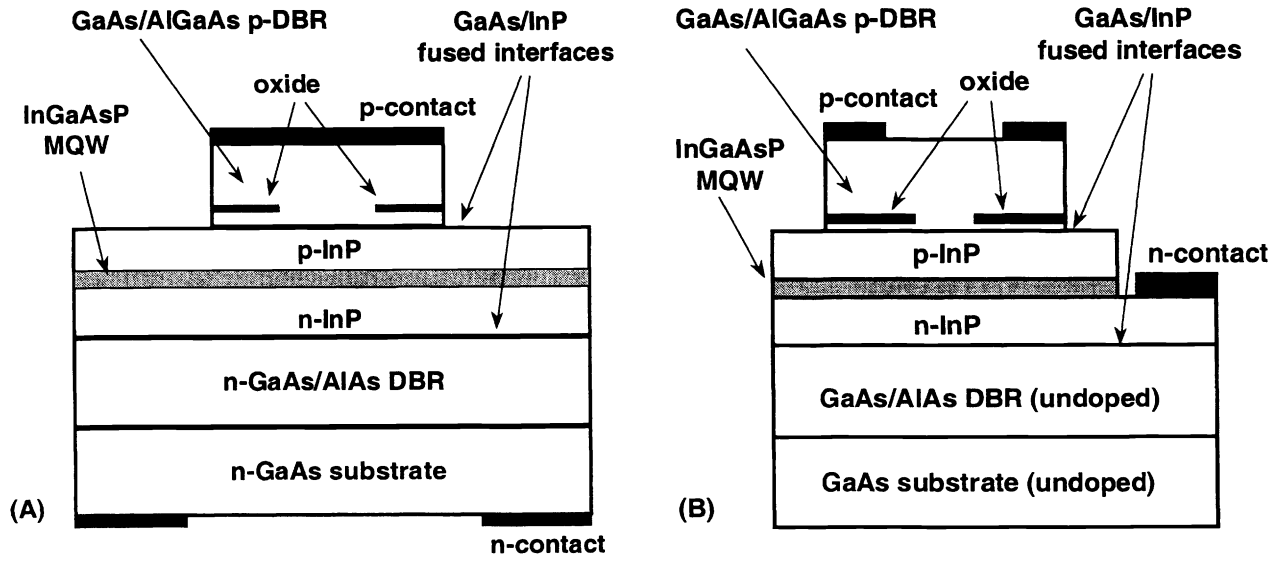

Fig. 1: Double-fused vertical-cavity lasers: (A) bottom emitting device, (B) top emitting device.

The energy band diagram is given in Fig.2 for both the devices. For three reasons, device B was expected to exhibit a better continuous-wave (cw) high-temperature performance than device A: (1) the lower electrical resistance of the top mirror leads to less self heating, (2) the p-side InGaP layer reduces electron leakage into the p-cladding at high temperatures, (3) the unstrained barriers reduce the (light) hole overflow from the quantum wells and thus intervalence band absorption.[11] Indeed, device B shows cw lasing at a record-high 71°C stage temperature,[9] a slight improvement of the previous record (64°C)[1] with device A.

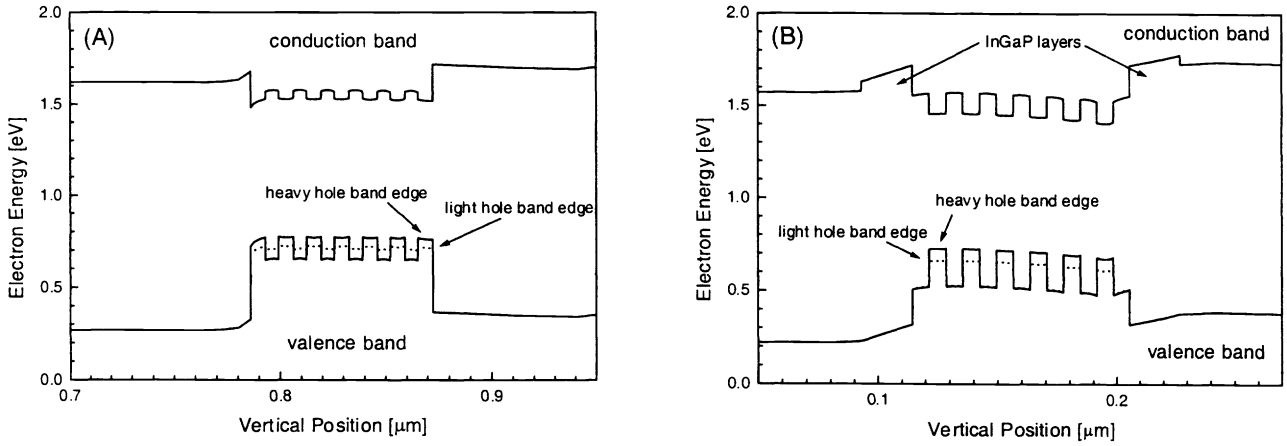

Fig. 2: Energy band diagram of the MQW active region for devices A and B (calculated near threshold).

3. THEORY

Regarding their analog modulation performance, the main differences between the two VCL types are expected to originate in their MQW active region design (Fig. 2). Device A employs tensile strain in the MQW barriers which leads to a small energy barrier for light holes (16meV) compared to 139meV in device B. The larger heavy-hole barrier shows a similar tendency: (A) 131meV, (B) 206meV. The electron barrier is (A) 43meV and (B) 114meV, respectively (all these numbers should not be confused with the larger bulk band offsets). These differences affect the optical gain not only via the carrier overflow effect but also via the overlap of the wave functions.[12] Deeper electron wells or more shallow heavy hole wells bring the overlap closer to unity and increase the optical gain. The reduced wave function overlap of well confined heavy holes and almost unconfined light holes in device A may reduce the valence band density of states and improve the differential gain.[12] On the other hand, the tensile strain in the barrier of device A can increase the gain compression factor ε.[13] We calculate the optical gain of both the strained MQWs utilizing an advanced laser simulation software.[14] A Lorentzian broadening function is used with 0.1ps intraband relaxation time. Band gap shrinkage due to carrier-carrier interaction is considered as $\Delta E_g = \sigma N^{1/3}$ with $\sigma = -10^{-12}$ eV/cm (N – average QW carrier density). The conduction bands are assumed to be parabolic and the non-parabolic valence bands are computed by the 4x4 **kp** method including valence band mixing.[15] The calculated gain of both the MQWs is plotted in Fig. 3 as function of carrier density N. At the peak of the gain spectrum (solid lines), device B shows superior gain properties. Considering the actual lasing wavelengths, the large offset from the gain peak in device B reduces its theoretical advantages (dashed lines). The gain dependence on carrier density N and photon density S can be approximately described by the following function[16]

$$g(N,S) = \frac{g_o}{1+\varepsilon S} \ln\left(\frac{N+N_s}{N_{tr}+N_s}\right) \qquad (1)$$

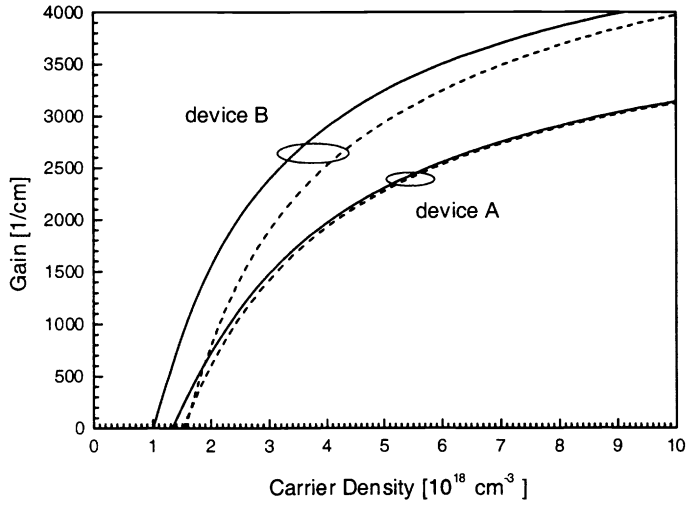

Fig. 3: Calculated gain vs. carrier density g(N) characteristics (solid: peak gain, dashed: gain at VCL emission wavelength).

Fitting the dashed curves of Fig. 3 gives (A) g_o=1168/cm, N_{tr}=1.56×10^{18}cm^{-3}, N_s=-0.97×10^{18}cm^{-3} and (B) g_o=1382/cm, N_{tr}=1.58×10^{18}cm^{-3}, N_s=-1.1×10^{18}cm^{-3}. The gain compression factor ε is assumed to be (A) 2.5×10^{-17}cm^3 and (B) 10^{-17}cm^3.[13] These numbers and Eq. 1 are used in the following two rate equations[17]

$$\frac{dN}{dt} = \frac{\eta_i I}{qV} - R(N) - g(N,S)v_g S \tag{2}$$

$$\frac{dS}{dt} = \left[\Gamma g(N,S) - \alpha(N)\right]v_g S + \beta\Gamma BN^2 \tag{3}$$

with

$$I(t) = I_{th} + I_{dc}[1 + M\sin(2\pi ft)] \tag{4}$$

$$R(N) = AN + BN^2 + CN^3 \tag{5}$$

$$\alpha(N) = \Gamma\kappa N + (1-\Gamma)\alpha_p + \alpha_m \tag{6}$$

including the injection efficiency η_i, the electron charge q, the QW active volume V, the photon group velocity v_g, the optical confinement factor Γ, and the spontaneous emission factor β. In Eq. 4, the injection current I(t) is composed of the threshold current I_{th}, the dc bias current I_{dc}, and the time-harmonic signal M×I_{dc}×sin(2πft) (M – electrical modulation depth, f - modulation frequency). The common Eq. 5 for quantum well recombination losses includes Shockley-Read-Hall (SRH) recombination (A=10^8/s), Auger recombination (C=10^{-28} cm^6/s), and spontaneous emission of photons (B=10^{-10} cm^3/s).[11] The modal photon loss coefficient α(N) includes constant contributions α_m from mirror transmission losses and (1-Γ)α_p from photon losses in passive layers. In addition, considerable QW absorption ΓκN is caused by intervalence band transitions and intraband transitions which both rise proportional to the carrier density, with κ = 35×10^{-18}cm^2.[18] This QW absorption slightly reduces the net differential gain

$$\frac{dg}{dN} = \frac{g_o}{1+\varepsilon S}\frac{1}{N+N_S} - \kappa \tag{7}$$

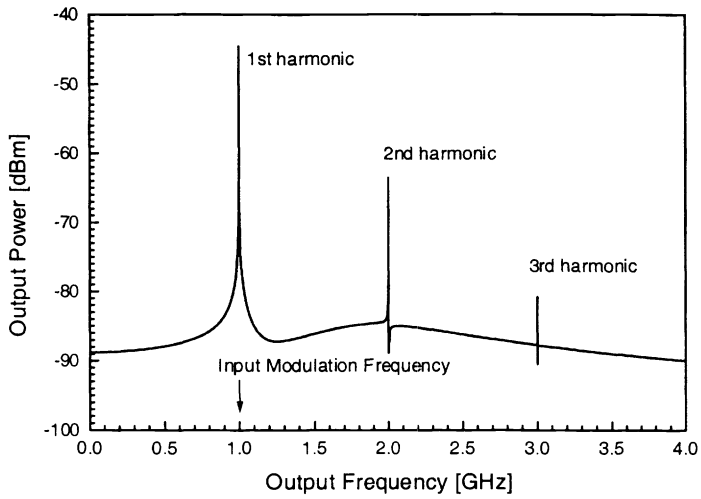

Fig. 4: Calculated ac output spectrum with f=1GHz modulation frequency (same simulation as in Fig. 8a with 5μm oxide aperture and with 1.8GHz resonance frequency; the Fourier transformation uses small 200kHz steps to keep the floor well below the 3rd harmonic peak).

Our model considers carrier recombination, photon losses, and gain in a less simplified way than usual[16] to better account for non-linear effects. However, we so far neglect the inhomogeneous distribution of photons and carriers[19, 20] as well as transport effects.[21] Thermal effects are reduced in our measurement by keeping the dc temperature constant. Internal and external parasitic effects are discussed in Sect. 4. Without any further simplification, we solve Eqs. 2 and 3 numerically in the time domain and apply Fourier transformation to obtain the ac output power spectrum for any given modulation frequency (Fig. 4). Recording the peak values of the three harmonics under variation of the modulation frequency f generates the curves in Fig. 5.

For comparison of devices A and B, we assume identical parameters I_{dc}=1mA, M=0.2, η_i=0.4, $\beta=6\times10^{-4}$ and an active region diameter of d_a=7μm in Fig. 5a. The low injection efficiency is mainly caused by current spreading at the fused p-side interface. Besides the different MQW properties given above, the two devices differ in the following parameters: the average DBR reflectivity R is (A) 0.998 and (B) 0.999 and the diameter of the optical mode d_{opt} is (A) 11μm and (B) 7μm giving a confinement factor Γ of (A) 0.013 and (B) 0.034 (including gain enhancement). From the measured threshold current I_{th} of (A) 5.5mA and (B) 3.1mA we deduce passive layer losses α_p of (A) 16/cm and (B) 63/cm. These somewhat surprising differences are related to the different mode confinement by the oxide layer which has been investigated by near field measurements. Device A exhibits an only weak mode confinement ($d_{opt}>d_a$)[1] correlated to low optical losses whereas the oxide layer in device B enforces a perfect mode confinement ($d_{opt}=d_a$) at even the lowest aperture diameters causing high scattering and diffraction losses.[19] At laser threshold, QW carrier densities N_{th} of (A) $3.8\times10^{18}cm^{-3}$ and (B) $3.3\times10^{18}cm^{-3}$ are calculated. The contribution of QW absorption to the internal loss $\Gamma\kappa N_{th}$ is (A) 1.6/cm and (B) 1.7/cm and it has only minor influence on the net differential gain dg/dN of (A) $3.7\times10^{-16}cm^2$ and (B) $6.1\times10^{-16}cm^2$ (see Fig. 3, Eq. 7). This large difference in dg/dN is caused by the MQW design and it is the main reason for the better high-speed performance of device B (solid lines in Fig. 5a). The predicted resonance frequency f_r is (A) 1.5 GHz and (B) 2.6 GHz. From small signal analysis,[16] the square of the resonance frequency is expected to be proportional to the dc current $I_{dc}=I-I_{th}$ (Eq. 8) and the factor b is a measure of the differential gain. We obtain from Fig. 5a (A) b=2.25 GHz^2/mA and (B) b=6.76 GHz^2/mA. Thus, the modulation efficiency is expected to be substantially improved in device B due to the higher differential gain dg/dN and the higher confinement factor. We discuss here the slope b rather than the –3dB bandwidth related parameter MCEF (≈1.55×√b) because our measurement is strongly affected by parasitic effects and by multimode lasing (see Fig. 6).

$$f_r^2 = b(I - I_{th}) \qquad b = \frac{1}{4\pi^2}\frac{dg}{dN}\frac{\Gamma v_g \eta_i}{qV} \tag{8}$$

Besides the laser output at the modulation frequency, Fig. 5a also shows the laser output at double (2^{nd} harmonic) and triple (3^{rd} harmonic) the input frequency f. Both the higher order harmonics exhibit a multi-peak structure which was not predicted by early studies of harmonic distortions.[22] The common peak at f_r is caused by the general enhancement of the output spectrum at resonance. Another peak should occur at $f_r/2$ and $f_r/3$ input frequency when the 2^{nd} and 3^{rd} harmonics output, respectively, is at the resonance frequency (see Fig. 4). In Fig. 5a, this peak is quite weak in case of the 3^{rd} harmonics and it is overshadowed by the 2^{nd} harmonics output resonance at $f_r/2$ which also enhances the 3^{rd} harmonic response. Fig. 5b shows the effect of gain compression by high photon densities (ε), spontaneous emission into the lasing mode (β), and QW absorbtion (κ) on the simulation results for device B. The first two effects are found to be of minor influence due to the low photon density ($8\times10^{13}cm^{-3}$) at our low dc current and due to the weak coupling factor $\beta=6\times10^{-4}$, respectively. QW absorption causes a somewhat lower resonance frequency due to the reduction in differential gain (Eq. 7).

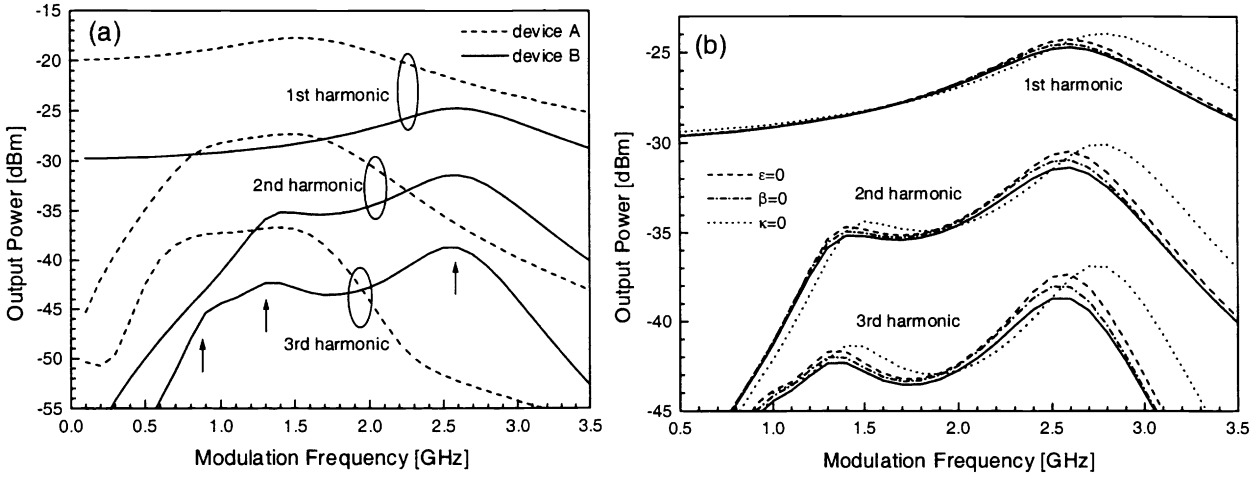

Fig. 5: (a) Simulated harmonics with 7μm oxide aperture (I_{dc}= 1mA, the arrows mark 3^{rd} harmonic peak positions $f_r/3$, $f_r/2$, and f_r of device B); (b) Effect of rate equation parameters on the harmonics of device B (solid: full simulation as in Fig. 5a).

4. EXPERIMENT

In the following we present analog modulation measurements of device B which are compared to experimental characteristics of device A published earlier.[1] The oxide aperture diameters d_{ox} investigated are 7μm (A and B) and 5μm (B only). Device B was packaged using 25 mil thick quartz with coplanar structure for microwave propagation. Short ribbon bonds connect the VCL to the package. The dc device temperature was kept constant at 15°C. The microwave signals are generated by a HP 8340B synthesized sweeper with a frequency range from 0.1 to 26.5 GHz. The microwave signal and the dc current are connected to the laser via a bias tee. A 6 dB attenuator is placed after the signal generator output to reduce signal reflections from the laser. The laser light is coupled into a single mode fiber through a Thor-Lab lens (numerical aperture 0.6). The fiber output is fed into a HP 70810A spectrum analyzer to characterize the analog signal received from the VCL. The measured spectrum looks similar to Fig. 4. The short emission wavelength of 1507nm prohibits the use of an Erbium doped fiber amplifier (EDFA) to increase the low output power of our devices.

Fig. 6 shows the fundamental harmonic response vs. modulation frequency f of device B at various dc currents. With the larger device (d_{ox}=7μm, Fig. 6a), single mode operation is only observed at the lowest current whereas the smaller device (d_{ox}=5μm, Fig. 6b) shows single mode lasing at all currents. Multi mode lasing is supported by the oxide index guiding which is stronger than in the single mode 7μm device A.[1] The existence of multiple modes gives rise to multiple peaks in the

first harmonic response[23] which make the theoretical analysis more difficult (see Fig. 6a). We first apply conventional small signal analysis using the general transfer function given in Eq. 9.[24] Both devices exhibit a low roll-off frequency f_L=2GHz (d_{ox}=7μm) and f_L=1GHz (d_{ox}=5μm), respectively, which seems to reflect external parasitic effects. Our 50μm wide ribbon wires have only about 1nH inductance which is too small to account for the low f_L. The contact pad capacitance is about C_p=0.5pF and it would give $f_p=(C_pR_d)^{-1}$=10GHz considering a differential VCL resistance of about R_d=200Ω. Thus, additional package effects might contribute. The not packaged device A had no contact pads and a roll-off frequency of 4.7 GHz (R_d=400Ω)[1] which results in 0.5pF parasitic capacitance. The maximum internal parasitic VCL capacitance is estimated to be about 1pF. Thus, future device designs for high-speed operation should reduce the parasitic capacitance. Such reductions led to more than 20 GHz bandwidth in oxide-confined 850nm VCLs.[7]

$$|M(f)|^2 = \frac{1}{1+\frac{f^2}{f_L^2}} \times \frac{f_r^4}{\left(f_r^2 - f^2\right)^2 + \left(\frac{\gamma f}{2\pi}\right)^2} \tag{9}$$

Small signal analysis (Eq. 9) of the fundamental harmonic response (Fig. 6) also gives the resonance frequency f_r(I) and the damping factor γ(I) which are plotted in Fig. 7. Results for device A[1] are added to Fig. 7a and the slope b of the function f_r^2(I) is in excellent agreement with the theoretical prediction of b=2.25 GHz^2/mA in Sect. 3. This confirms our rate equation model as well as the gain analysis. The good agreement also excludes any significant influence of hole transport effects which could contribute to the low-frequency roll-off. Those transport effects would reduce the resonance frequency.[21] As predicted, the modulation efficiency is substantially improved in device B (Fig. 7a, d_{ox}=7μm). However, the theoretical slope b=6.76 GHz^2/mA is higher than measured which is mainly due to the existence of multiple modes in the experiment reducing the confinement factor Γ. With shrinking oxide aperture, device B shows the expected improvement of the modulation efficiency.

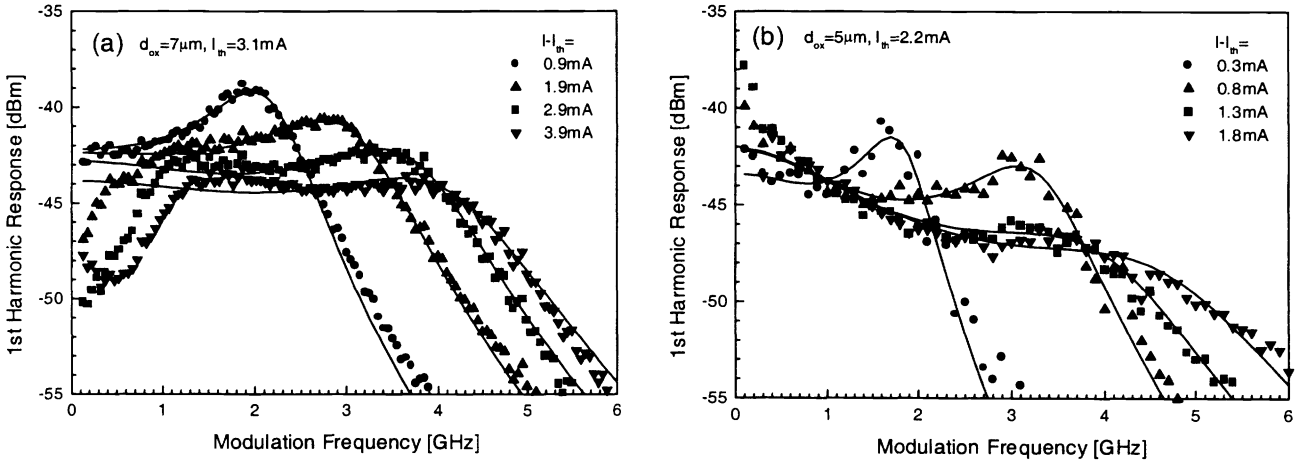

Fig. 6: Measured modulation response of device B at different dc currents with an oxide aperture diameter of (a) 7μm and (b) 5μm. The solid lines give the result of small signal analysis using Eq. 9.

Fig. 7b gives the damping constants which are expected to follow $\gamma = K \times f_r^2 + \gamma_o$.[16] The constant γ_o is close to the differential carrier recombination rate dR/dN and 1/K is proportional to the optical losses α(N).[16] The K-factor is often used to estimate the intrinsic (maximum) modulation bandwidth $f_{max}=2\pi\sqrt{2}/K$.[16] The linear fit in Fig. 7b gives f_{max}= 19 GHz for the larger VCL and 13 GHz for the smaller VCL (device A: 24 GHz)[1]. The relatively strong intrinsic damping in all our devices may be mainly attributed to the strong MQW Auger recombination and the wide current spreading at the fused p-type interface.

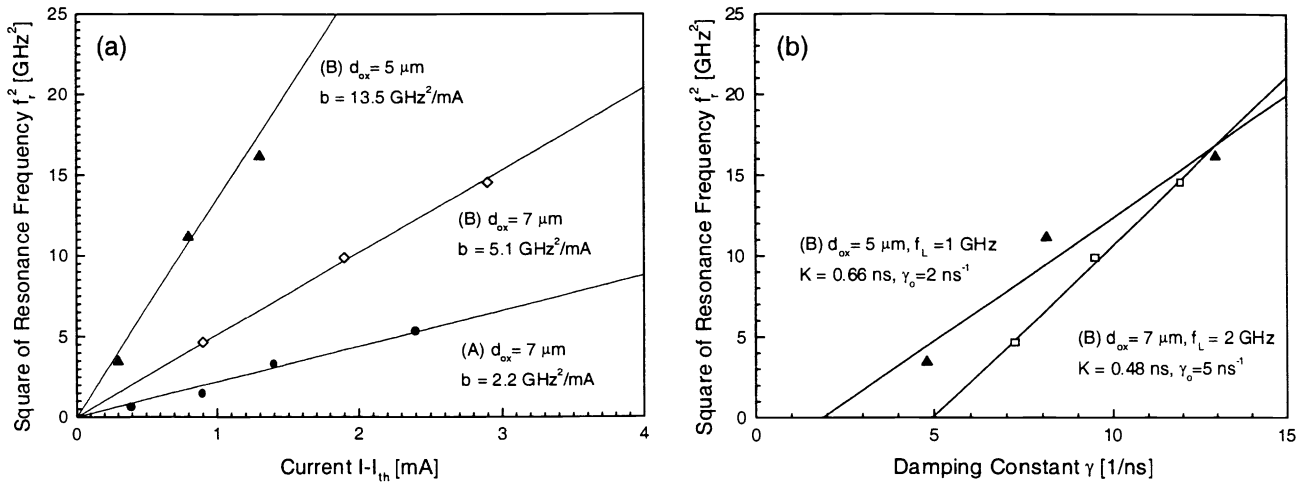

Fig. 7: Square of measured resonance frequencies (a) versus dc current I-I_{th} = f_r^2/b and (b) versus damping constant $\gamma = K \times f_r^2 + \gamma_o$. (all data point of device B are from small signal analysis of Fig. 6 , full dots indicate single mode operation).

In the following, we investigate harmonic distortions of device B with 5μm oxide aperture. Fig. 8a shows the measured (dots) and the simulated (lines) modulation response of the first three harmonics. Measurement and rate equation simulation are in excellent agreement except at high frequencies due to the parasitic roll-off which is not included in the model. This agreement confirms that the measured non-linearity is mainly caused by intrinsic electron-photon interactions. Slight deviations are related to the non-linearity of the light power vs. current (LI) characteristic at low currents (Fig. 8b). At higher currents, the LI curve is more linear but the harmonics peaks near resonance deteriorate due to parasitic roll-off. In Fig. 8a, the measured plateau of the 2nd harmonic is close to the simulation with predicted peaks at f_r=1.8GHz and f_r/2=0.9 GHz. As simulated, the third harmonic shows a main peak at about f_r/3=0.6 GHz (hiding another peak at f_r/2) and a smaller peak at f_r.

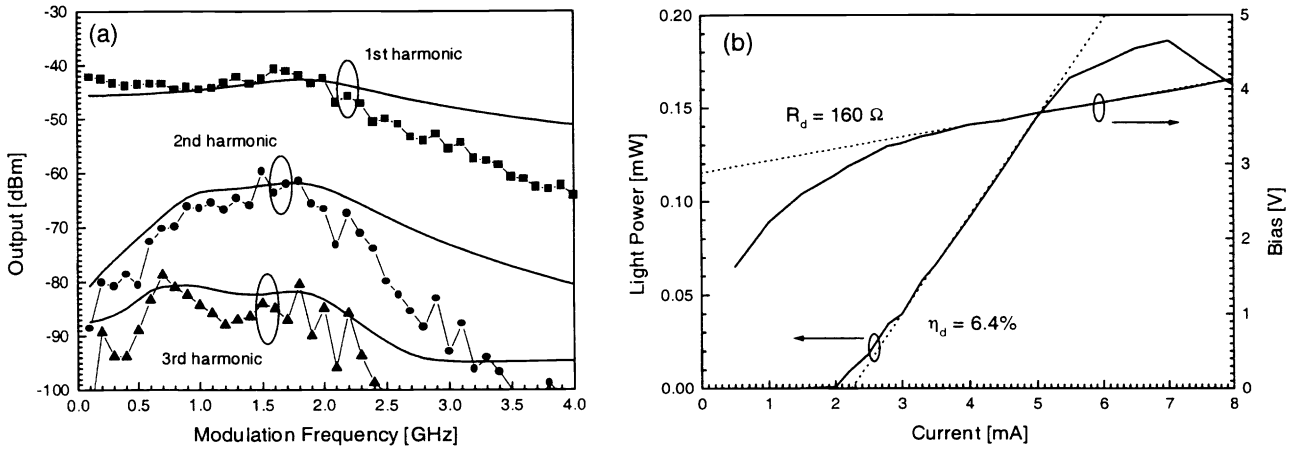

Fig. 8: Characteristics of device B with d_{ox}=5μm: (a) modulation response at output frequencies f, 2f, and 3f (I=2.5mA, M=0.02, dots - measurement, lines - rate equation simulation results); (b) measured light vs. current (LI) and voltage vs. current (VI) curve without temperature stabilization (η_d - differential quantum efficiency, R_d – differential resistance).

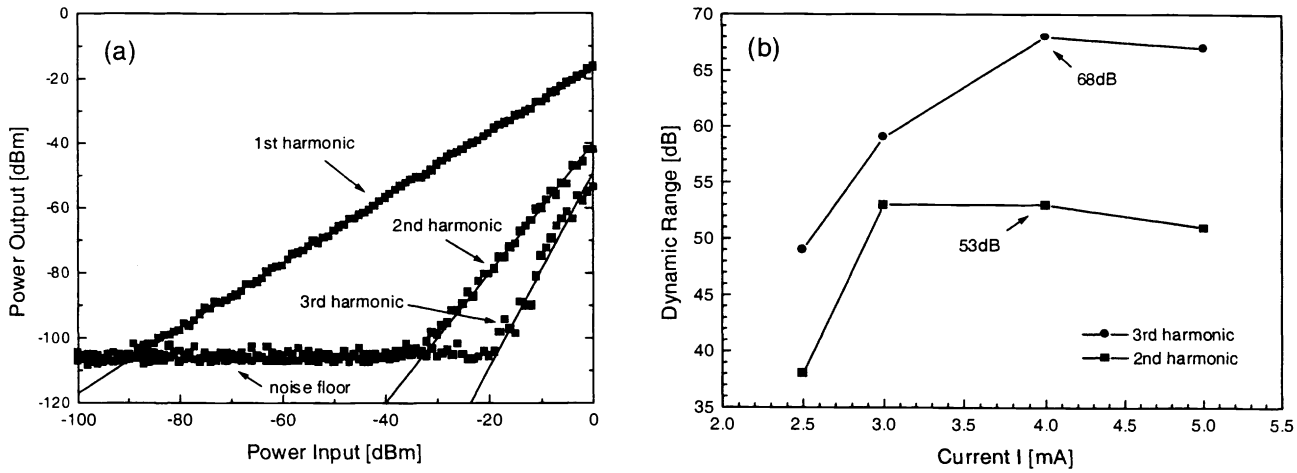

Fig. 9: Measured characteristics of device B with d_{ox}=5μm at 1GHz modulation frequency: (a) Output power of the three harmonics vs. input power (I=4mA, lines indicate slope 1, 2, and 3, resp.); (b) maximum distance of the higher harmonics to the 1st harmonic response as function of current.

Fig. 9a shows the effect of changing the modulation depth M at I=4mA. 1st, 2nd, and 3rd order harmonics, respectively, are expected to be the first components of a power series $P_{out} = a_1 P_{in} + a_2 P_{in}^2 + a_3 P_{in}^3 + \ldots$ with P_{in} being the input ac signal power and P_{out} being the total ac output power. This expectation is confirmed by the three straight lines of slope 1, 2, and 3, respectively, in Fig. 9a. Their intersection points with P_{in}=0dBm give the a-coefficients of the power series. The maximum distance between fundamental and higher order harmonic response (dynamic range) is about 53dB (2nd harmonic) and 68dB (3rd harmonic), respectively, and it is limited by the noise floor which corresponds to the 50Hz measurement bandwidth of the spectrum analyzer. The 3rd harmonic dynamic range is close to previous results on third order intermodulation distortion (69dB measured on device type A with d_{ox}=14μm)[4] which translates into 80 dB $Hz^{2/3}$ spurious free dynamic range (1 Hz measurement bandwidth).[25] The dynamic range depends on the dc current (Fig. 9b). It is reduced at lower currents since the modulation frequency of 1 GHz comes close to the peaks of the higher harmonics (Fig. 8a). The dynamic range is expected to be larger at lower modulation frequencies.

5. SUMMARY

In summary, we have demonstrated a substantial improvement of optical gain, mode confinement, and modulation resonance frequency compared to our previous 1.55μm vertical-cavity lasers. This improvement is mainly achieved by reducing the MQW barrier strain and by strengthening the wave guiding by the oxide layer. The differential gain at threshold ($dg/dN=6\times10^{-16}cm^2$) is 1.6 times higher and the optical confinement factor (Γ=0.034) is 2.6 times higher than in previous devices. This results in an improvement of the modulation current efficiency by a factor of about 1.7. However, the modulation bandwidth of our new devices is strongly limited by parasitic effects. Future designs of device, contacts, and package need to reduce the parasitic capacitance. Second and third order harmonic distortions are found to exhibit multiple peaks as the modulation frequency changes. One peak occurs when the specific output frequency hits the fundamental resonance frequency. Other peaks occur whenever a lower order harmonic response is at resonance. The measured non-linearity of the ac laser output is mainly caused by intrinsic electron-photon interaction within the quantum wells. A maximum dynamic range of, respectively, 53dB (2nd harmonic) and 68dB (3rd harmonic) is measured.

ACKNOWLEDGEMENT

The authors appreciate the support of DARPA (Dr. Leheny) and Rome Labs (Mr. Tsacoyeanes) in this research. Assistance with the experimental setup from Jon Wesselmann and useful discussions with Charlie Cox are gratefully acknowledged.

REFERENCES

[1] N. M. Margalit, J. Piprek, S. Zhang, D. I. Babic, K. Streubel, R. P. Mirin, J. R. Wesselmann, J. E. Bowers, and E. L. Hu, "64°C continuous-wave operation of 1.5 μm vertical-cavity laser," IEEE J. Sel. Top. Quantum Electron., vol. 3, pp. 359-365, April 1997.

[2] S. Z. Zhang, N. M. Margalit, T. E. Reynolds, and J. E. Bowers, "1.55μm vertical-cavity laser transmission over 200km at 622Mbit/s," Electr. Lett., vol. 32, pp. 1597-1599, August 1996.

[3] S. Z. Zhang, N. M. Margalit, T. E. Reynolds, and J. E. Bowers, "1.54μm vertical-cavity surface-emitting laser transmission at 2.5 Gb/s," IEEE Phot. Techn. Lett., vol. 9, pp. 374-376, March 1997.

[4] J. R. Wesselmann, , N. M. Margalit, and J. E. Bowers, "Analog measurements of long wavelength vertical-cavity lasers," Appl. Phys. Lett., vol. 72, pp. 2084-2086, April 1998.

[5] O. Kjebon, R. Schatz, S. Lourdudoss, S. Nilsson, B. Stalnacke, and L. Backbom, "30GHz direct modulation bandwidth in detuned loaded InGaAsP DBR lasers at 1.55μm wavelength," Electr. Lett., vol. 33, pp. 488-489, March 1997.

[6] K.L. Lear, A. Mar, K.D. Choquette, S. P. Kilcoyne, R. P. Schneider, and K. M. Geib, "High-frequency modulation of oxide-confined vertical-cavity surface emitting lasers," Electr. Lett., vol. 32, pp. 457-458, February 1996.

[7] K. L. Lear, M. Ochiai, V. M. Hietala, H. Q. Hou, B. E. Hammons, J. J. Banas, and J. A. Nevers, " High-Speed Vertical-Cavity Surface-Emitting Lasers," 1997 Digest IEEE/LEOS Summer Topical Meetings, Vertical-Cavity Lasers, pp. 53-54, 1997.

[8] D. Tauber , G. Wang, R. S. Geels, J. E. Bowers, and L.A. Coldren, " Large and small signal dynamics of vertical cavity surface emitting lasers," Appl. Phys. Lett., vol. 62, pp. 325-327, January 1993.

[9] K.A. Black, P. Abraham, N.M. Margalit, E.R. Hegblom, Y.-J. Chiu, J. Piprek, J.E. Bowers and E.L. Hu, "Double-fused 1.5-micron vertical cavity lasers with record high To of 132K at room temperature," Electron. Lett., vol. 34, pp. 1947-1949, 1998.

[10] L. Zhang and D.A. Ackermann, " Second- and third-order harmonic distortion in DFB lasers'" IEEE J. Quant. Electr., vol. 31, pp.1974-1980, November 1995.

[11] J. Piprek, D. Babic, and J. E. Bowers, "Simulation and analysis of double-fused 1.55μm vertical-cavity lasers," J. Appl. Phys. **81**, pp. 3382-3390, 1997.

[12] Y. Matsui, H. Murai, S. Arahira, Y. Ogawa, and A. Suzuki, " Novel Design Scheme for High-Speed MQW Lasers with Enhanced Differential Gain and Reduced Carrier Transport Effect," IEEE J. Quant. Electr., vol 34, pp. 2340-2349, December 1998.

[13] S. Bouchoule, C. Kazmierski, D. Mathoorasing, A. Ougazzaden, and J.-Y. Marzin, "Barrier strain influence on the high speed properties of compressively strained InGaAsP multiquantum well laser structures," IEEE J. Select. Topics Quantum Electr. Vol. 3, pp. 330-335, April 1997.

[14] PICS3D 4.1.2 by Crosslight Software, Inc. (user manual available on the internet at www.crosslight.ca)

[15] S. L. Chuang, "Efficient band Structure calculations of strained quantum wells," Phys. Rev. B, vol. 43, pp. 9649-9661, 1991.

[16] L. A. Coldren and S. W. Corzine, *Diode Lasers and Photonic Integrated Circuits,* Wiley, New York, 1995.

[17] A. A. Bernussi, J. Pikal, H. Temkin, D. L. Coblentz, and R. A. Logan, " Rate equation model of high-temperature performance of InGaAsP quantum well lasers," Appl. Phys. Lett., vol. 66, pp. 3606-3608, 1995.

[18] Joindot and J.L.Beylat, "Intervalence band absorption coefficient measurements in bulk layer, strained and unstrained multiquantum well 1.55 μm semiconductor lasers," Electron. Lett. **29**, pp.604-606, 1993.

[19] S. F. Yu, W. N. Wong, P. Shum, and E. H. Li, "Theoretical Analysis of Modulation Response and Second-Order Harmonic Distortion in Vertical-Cavity Surface-Emitting Lasers," IEEE J. Quant. Electr., vol. 32, pp. 2139-2147, December 1996.

[20] N. Tessler and G. Eisenstein, "On Carrier Injection and Gain Dynamics in Quantum Well Lasers," IEEE J. Quant. Electr., vol. 29, pp. 1586-1593, June 1993.

[21] R. Nagarajan, "Carrier transport effects in quantum well lasers: an overview," Opt. Quant. Electr., vol. 26, pp. S647-S666, 1994.

[22] T. E. Darcie, R.S. Tucker, and G. J. Sullivan, "Intermodulation and harmonic distortion in InGaAsP lasers," Electron. Lett., vol. 21, pp.665-666, August 1985.

[23] Y. Satubi and M. Orenstein, " Small-Signal Modulation of Multitransverse Modes Vertical-Cavity Surface-Emitting Lasers," IEEE Phot. Techn. Lett., vol. 10, pp.757-759, June 1998.

[24] R. Nagarajan, T. Fukushima, J. E. Bowers, R. S. Geels, and L.A.Coldren, "High-Speed InGaAs/GaAs strained multiple quantum well lasers with low damping," Appl. Phys. Lett., vol. 58, pp. 2326-2328, May 1991.

[25] R. V. Dalal, R. J. Ram, R. Helkey, H. Roussell, and K. D. Choquette, " Low distortion analogue signal transmission using vertical cavity lasers," Electr. Lett., vol. 34, pp. 1590-1591, August 1998.